A reverse identification of the friction coefficient operating within crack lips through a complete elastoplastic simulation of 3D fretting fatigue cracks

P. Arnaud, V. Maurel, Siegfried Fouvry, J. Said, C. Yang, Fikri Hafid

A reverse identification of the friction coefficient operating within crack lips through a complete elastoplastic simulation of 3D fretting fatigue cracks.

P. Arnaud [1], V. Maurel[1], S. Fouvry[2], J. Said[3], C. Yang[3], F. Hafid[3]

1 MinesParis, PSL University, Centre for material sciences (MAT), UMR 7633 CNRS, 91003 Evry, France

2 Ecole Centrale de Lyon, LTDS Laboratory, 36 av Guy de Collongue, 69130 Ecully, France

3 RTE – Direction de la R&D – Pôle Smartlab, 92073, Paris la Defense Cedex, France

Abstract

This study investigates the fretting fatigue cracking process through elastic and elastoplastic simulations of former tests. Tests were performed to characterize the friction coefficient for used the aluminum alloy used for representative conditions. Then, three-dimensional finite element simulations, incorporating 3D cracks within the contact, were conducted to replicate the experiments to compare the former results. Notably, it was shown that the elastic assumption fails to capture the threshold crack extension, which would result in systematically underestimated crack arrest lengths. The study emphasizes the necessity of elastoplastic simulations to understand the process of fretting fatigue crack propagation and highlights the importance of considering complex multiaxial loading conditions for accurate assessments. Finally, Plastic simulations, considering for steady-state conditions, demonstrated SIF evolution consistent with experimental observations explaining that the crack arrest occurs due to friction in the crack lips. Through a reverse analysis, the friction coefficient operating within the crack lips was extrapolated, yielding a value consistent with measurements from gross slip fretting experiments.

1. Introduction

Fretting is a type of mechanical loading that involves oscillating friction and displacement that is always smaller than the contact area. Fatigue, on the other hand, is also a type of mechanical loading involving oscillating forces that can lead to crack initiation, growth and failure. Both phenomena can be found in many industrial applications and the lifetime of these systems is often determined by these types of loading [1]. In a wire rope, for example, there are many contact points between the wires that can lead to fretting fatigue failure [2-5]. In order to detect cracks and maintain these systems effectively, it is important for companies to understand and predict the damage that can be caused by fretting fatigue. Overhead conductors consist of several layers of helically stranded wires, with inner steel wires to support the loadings and outer aluminum wires to conduct the current (fig. 1). Under the action of external loadings such as wind, contact and friction occur between the wires. The contact shape is elliptical due to the cylinder/cylinder configuration with a crossing angle but with a plasticity that greatly increases the contact size and reduces pressures. At the same time, fatigue occurs in the wire due to conductor vibration, both of which can lead to fretting fatigue. Eventually, due to the cyclic propagation of cracks caused by contact conditions, failure can occur and affect the electrical power system. Lifetime reduction due to this damage has been reported in the literature [6-10]. Furthermore, the authors were particularly interested in the clamping region, where most failures have been observed due to high contact pressures. In previous work, an experimental and numerical strategy has been developed to predict the risk of cracking around the clamped zone subjected to both clamping force and oscillating bending motion [2,10,11]. By explicitly modeling the crack, it was clarified for an elastic mechanical behavior how SIF values for opening and shear modes compete within the contact. Surprisingly, the authors [11] conclude that the crack was closed (zero value, or negative SIF values reached in mode I as a function of contact assumptions), despite the crack growth observed in experiments. This point is crucial in order to elaborate the loading condition for which crack arrest is reached or on the opposite the condition of crack propagation and final failure of the system. First, the investigated material, a quasi-pure Aluminum,

shows almost plastic behavior with a low yield stress level, due to the lack of hardening phases. This implies that crack growth could be influenced by stress redistribution in the presence of plasticity where large-scale yielding is observed within the contact. This raises the question of the extent to which plasticity could influence crack tip behavior.

Secondly, in this previous study [10], the authors only considered a given crack geometry, whereas modelling cracks and their evolution, by methods such as the extended finite element method (X-FEM) or conformal remeshing, are particularly useful to gain in clarification of the redistribution of stress during crack propagation. Many successful applications of this finite element analysis (FEA) crack simulation process have been demonstrated, particularly in the context of linear elastic fracture mechanics (LEFM) based on G-θ analysis [13,17]. Basically, a Paris' like law is derived from SIF or J assessment, so as to evaluate locally the crack increment. Moreover, these methods allow a better understanding of crack propagation and crack arrest under multiaxial and plasticity conditions, which are always challenging issues [12, 18, 19].

Due to large scale yielding conditions within the contact and the crack growth, when dealing with FEA accounting for crack growth, field transfer operations should be performed in the case of such elasto-plastic behavior to obtain a relevant stress state. This point has been carried out for conformal remeshing techniques by a systematic transfer of internal variables from the Gauss and nodal points in the mesh before crack increment, to the nearest Gauss and nodal points or by interpolation in the mesh after crack increment and subsequent remeshing step [12-16].

One aim of this paper is to understand how the normal force between the wires could affect the crack arrest phenomenon and to achieve a robust assessment of the mechanical condition yielding crack arrest based on finite element method. Experimental results are presented to detail the condition of crack arrest focusing on the evaluation of the coefficient of friction (COF) between the wires. From a numerical aspect, FEA of the contact between two wires is studied considering for the growth of a 3D crack within the contact. The coupling between crack growth, crack arrest and local

loadings for high plasticity conditions will be detailed. From this investigation, a reverse analysis is proposed to identify the COF operating between the crack lips.

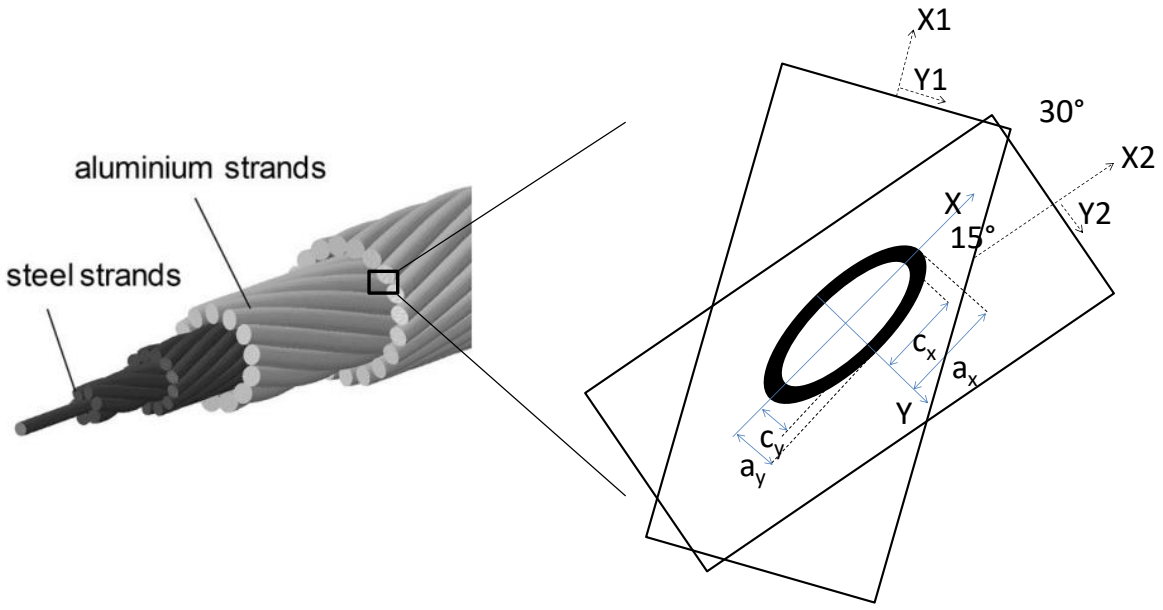

Figure 1: conductor structure and generated elliptical contact between wires.

2. Studied material.

The studied material consists of a quasi-pure aluminum with a composition of up to 99% Al. This composition was chosen to guarantee very high electrical conductivity but at the expense of very weak mechanical properties [15]. After casting, this metal was rolled into the shape of a bar, then bars were passed through a series of drawing dies with progressively smaller internal diameters in order to gradually reduce the wire diameter until it reaches its target final size. The current work focuses on a particular conductor geometry with a 3.6 mm diameter. In a previous study [20], the aluminum microstructure was analyzed by electron backscatter diffraction (EBSD) and mechanical tests (tensile and fretting). The EBSD analysis displays a partially oriented microstructure in the <111> orientation and a recrystallization classically observed in the literature [21,22]. Observations of misorientation within each grain reveal no significant deformation and the microstructure is partially oriented. With this observation, the mechanical properties are assumed to be isotropic, and the

elastoplastic (EP) properties were determined according to a non-linear isotropic and kinematic hardening Chaboche law [23]:

$$f\left(\underline{\underline{\sigma}}\right) = J\left(\underline{\underline{\sigma}} - \underline{\underline{X}}\right) - R_0 - R(p) \quad (1)$$

where $\underline{\underline{X}}$ and R correspond to the kinematic tensor and isotropic strain hardening, respectively, R_0 is the elastic limit, and p the plastic multiplier. Hardenings are assessed through partial differential equations as follows:

$$\dot{\underline{\underline{X}}} = \frac{2}{3} C \dot{\underline{\underline{\varepsilon}}}_p - D\underline{\underline{X}} \quad (2)$$

$$and \quad \dot{R} = b(Q - R)\dot{p} \quad with \quad R = Q(1 - \exp(-bp)) \quad (3)$$

These EP cyclic parameters were identified from an optimized reverse analysis including cycle tension compression experiments but also dedicated fretting tests by comparing the contact size extension [20].

Table 1: set of elasto-plastic parameters obtained in [20] including constant isotropic and a Chaboche law [23]

E (GPa)	v	C (MPa)	D (s^{-1})	b (MPa)	Q	R_0 (MPa)
65	0.345	44000	460	13	60	75

3. Experimentation

3.1. Tests of coefficient of friction

The aim of the tribological tests is to obtain information about the COF involved in the contact between the crack lips. Plain fretting tests were carried out between two crossed wires to evaluate this behavior. To mimic the contact arrangement between the two wires in the conductor, a 30° angle is applied in these plain fretting tests. While the first specimen is being moved by a hydraulic

actuator at a constant 10 Hz frequency, the second specimen is fixed. The apparatus is shown in Figure 2. A normal load (P) is applied by a spring system between supports and the specimen displacement is prescribed as a function of time δ(t) producing a tangential force Q(t). The tangential force is measured by MTS sensor while the displacement is measured by the LVDT actuator. Both measurements are used to plot the Q – δ fretting cycle, from which the COF is deduced using the tangential force Q*. Frequency, amplitude, atmosphere, and normal load are test parameters that have a significant effect on the COF. This coefficient presents a challenge in terms of accurate characterization, thus highlighting the importance of closely approximating the conditions in which the conductor operates when assessing it.

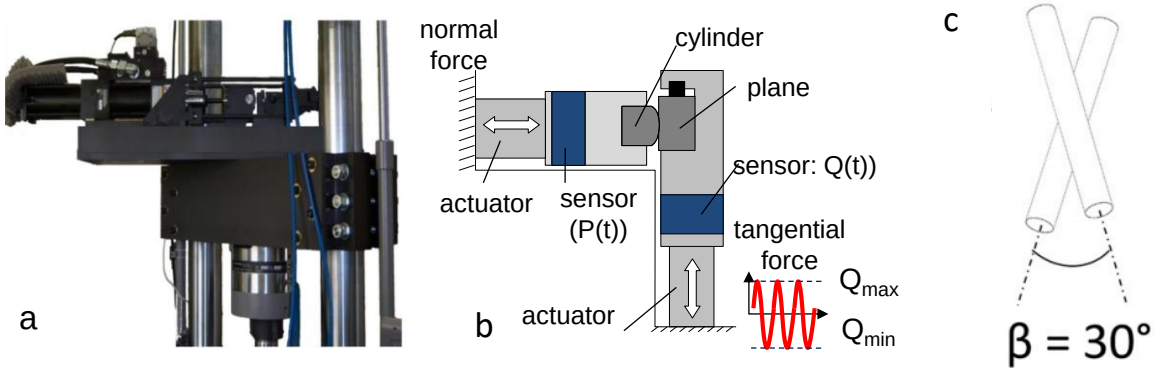

Figure 2: a) device used for characterizing COF, b) schematic representation of the device; c) representation of the contact with 30° angle.

Tests were carried out to investigate two aspects of friction. The first aspect is the partial/gross slip transition coefficient μ_t, which, as its name suggests, describes the transition between the partial slip region and the total slip domain. The protocol used to measure the transition coefficient is the variable displacement test performed with a constant normal load P by Voisin [24].

The rate of increase of the tangential displacement amplitude is set at 5000 cycles for each level of displacement amplitude to allow the contact to stabilize. Three normal forces are investigated, 80, 140 and 200 N, and three tests are performed for each condition. The tangential load amplitude is

measured as a function of the displacement amplitude. The contact remains in partial slip until a Q_t value corresponding to the transition from partial to total slip is reached. It is then possible to determine the COF in a slip state when the slip transition is reached. The decrease in the COF after the slip transition can be attributed to wear, which is induced by the increase in slip creating a layer of debris at the interface which acts as a lubricant. However, the studied material has weak plastic properties. In fact, lateral plastic protusions have been observed experimentally: plowing effect has been measured by 3D profilometer (Fig. 3c). These plastic protusions play an important role in the measurement of the sliding COF, adding a component to the measured COF. The apparent COF μ_{app} is thus composed of a true COF μ_{true} and a plowing coefficient μ_{plow}: $\mu_{app} = \mu_{true} + \mu_{plow}$ [25,26]. The plastic protusions can also have an important influence on the transition coefficient μ_t, indeed it must be deformed in order to start sliding. One way of estimating the true COF is to use the energetic COF through the distribution of energy over the sliding distance, which means that the calculated value is slightly higher than the true COF:

$$\mu_e = \frac{E_d}{4 * \delta * P}$$

where E_d is the dissipated energy during one cycle, δ is the sliding amplitude during one cycle and P is the normal force. It should be noted that the assessment of the COF μ and μ_e is only valid under gross slip conditions. Under partial slip condition, since part of the tangential loading results of the stick zone accommodation, the COF cannot be derived from this global analysis of tangential force and friction energy parameters. Then to assess μ_{te}, the observed value read just after the transition is used.

Figures 3 a) and b) show the measured (apparent) and energetic transition and the sliding COFs. The energetic friction coefficients μ_e are on average ~40% lower than the measured ones. Here the role of plasticity through a plowing effect is important. The COFs do not seem to depend on the normal force in the studied domain.

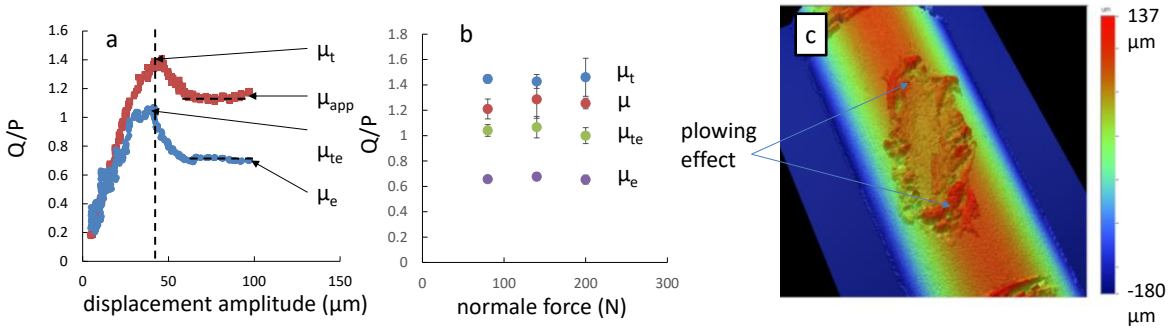

Figure 3: a) evolution of the measured and energetic COF as a function of the displacement amplitude; b) evolution of the COF as the function of the normal force; c) topologic observation of plowing effect.

3.2. Experimental crack arrest investigation through normal force

To determine the crack arrest condition, fretting fatigue tests have been performed in previous work [11] and are therefore briefly described. The hydraulic fretting fatigue bench used for this work has a dual actuator configuration, it is designed to study various behaviors by controlling fretting and fatigue independently. The frequency was set to 10 Hz for 10^7 cycles. The samples were located at β=30° degree, which is consistent with both the industrial application and the COF study described above. The fatigue sample is vertical, and the strand of the fretting strand contact is shorter and positioned with the 30° angle as observed in industrial case. To prevent bending, a PTFE counter-body is placed on the opposite side of the fatigue sample. While the lower actuator applies the fatigue load, the magnitude of the fretting displacement δ(t) is manually increased until the tangential force Q* reaches the target value.

Two sets of tests were used in this work, Figure 4 shows the lifetime evolution of the fretting fatigue test for 2 tangential force amplitudes Q* as a function of normal force P, for a fatigue stress of σ_{fat}=60 MPa with a fatigue ratio of R_{fat}=0.5. All the observed fractures tests occur in the contact area and crack nucleation for unbroken tests, could also be observed in this area. An increase in normal force, keeping all other parameters held constant, can delay or prevent strand failure. For values of P

lower than the normal force at crack arrest, P_{CA}, the evolution of the lifetime appears to be stable and independent of P. As the P_{CA} is approached, the number of cycles to failure increases rapidly and finally beyond the threshold value P_{CA}, the lifetime is greater than 10^7 cycles. This particular behavior suggests that the increase in normal force and therefore hydrostatic pressure may lead to crack arrest and/or crack closure effects.

It is interesting to note that as P decreases below P_{CA}, the lifetime asymptotically decreases to a plateau value around 3.10^6 regardless of the tangential force applied (150 or 200 N). Note that the normal force cannot be reduced below a threshold value modifying the contact condition. In summary, two interesting results are found: the P_{CA} values describe a crack arrest phenomenon with P_{CA}=300 N for Q*=150 N and P_{CA}=450 N for Q*=200 N and the lifetime value tends to 3 10^6 cycles for P< P_{CA}.

a

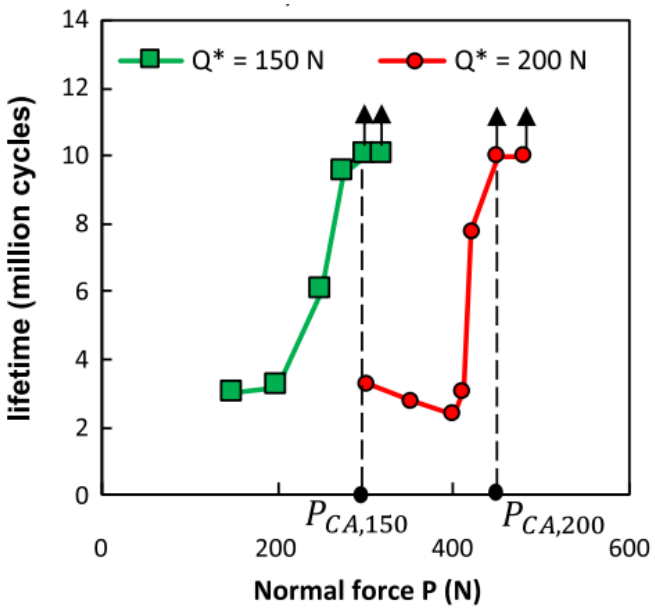

b

Figure 4: a) fretting fatigue test used for the analysis; b) lifetime in fretting fatigue as a function of contact normal force for two tangential force values of Q*=150 N and 200 N with wire/wire contact of 3.6 mm in diameter at 10 Hz σ_{fat}=60 MPa. [11]

Further post-processing analysis of non-failed specimens also revealed that the associated crack was located near the contact edge, with depths ranging from 170 to 250 µm (Fig. 5). This result is very interesting because it shows that the cracks were initiated at force values higher than P_{CA} but without crack propagation. Thus, the observed crack arrest is due to normal force. These observations also highlight the angle α between the crack and the surface, which is of about 30°, Figure 5. This angle is very small and characterizes the direction of the crack under the contact. This crack orientation, far from the plane orthogonal to the fatigue stress direction, tends to show that the crack is initiated in mode II and propagates with the same orientation. This consistency between the different post-processed cracks allows us to establish a typical crack geometry corresponding to the crack arrest condition: projected crack length at crack arrest condition b_{CA}= 200 µm, and crack angle α = 30° and an angle of about 15 degrees is observed with respect to the axis of the wire direction. This orientation is probably due to the 30° degree angle between the strands which induces a crack initiation This geometry will be used in the following sections.

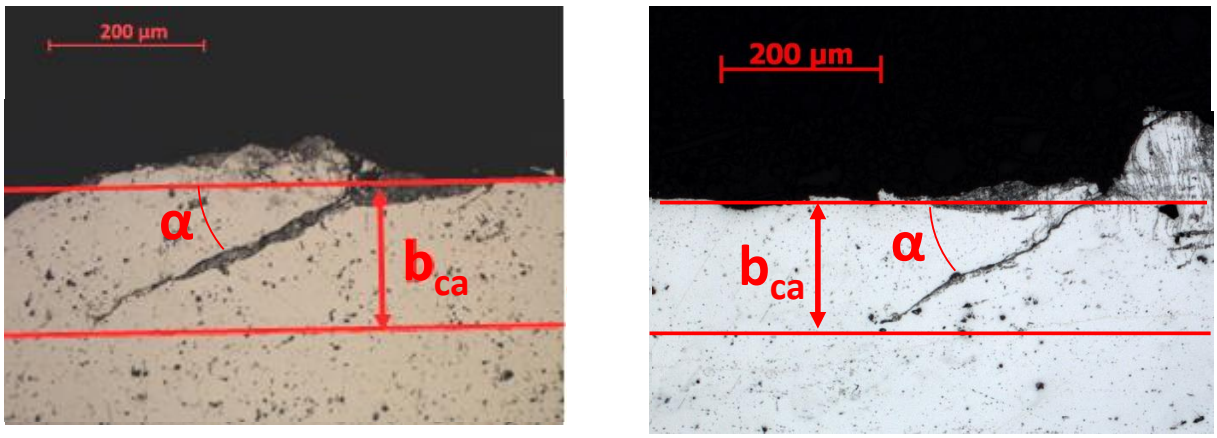

Figure 5: Optical observation of cross-section highlighting crack arrest a) for the condition P=300 N, Q*=150 N and F=70 MPa; and b) for the condition P=450 N, Q*=200 N and F=70 MPa.

4. Finite element modeling of crack in fretting fatigue loading

4.1. Finite element model

The finite element model developed in this study is similar to the one presented in [20]. Figure 6 shows the Abaqus 3D fretting model between the crossed wire contact using hybrid linear elements. These elements limit the computational time and are known to provide a reliable assessment of the hydrostatic pressure generated by the contact and to improve the plasticity results. Each node of this element has 3 degrees of freedom (dof) for displacement and an additional one to ensure convergence of the pressure, and the trace of stress tensor. Using 3D tetrahedral elements with this additional dof for pressure convergence, C3D4H element in Abaqus, the number of dof per element is of 13. The wire length is 12 mm and the angle between the wires is set to 30°, in accordance with the test configuration. The model is composed of two half-wires consisting of a cylindrical surface in contact with each other and 3 flat surfaces used to impose loads and boundary conditions (figure 6). For wire #2, an embedding condition is applied to one of its two semicircular surfaces, while a fatigue stress condition is applied to the other. A symmetry condition is enforced on the rectangular surface. As with wire #1, the three surfaces are linked to a multi-point constraint (MPC) to control the wire. This constraint controls both normal and tangential forces.

To bring some new understanding in the context of plastic behavior, a purely linear isotropic elastic hypothesis (E) is first considered as a reference case. The EP case combines linear isotropic elastic behavior and plastic behavior. This behavior combines non-linear isotropic and kinematic hardening terms. It was identified in a previous study, where inverse analysis was promoted [20]. The selected parameters are presented in part 2.

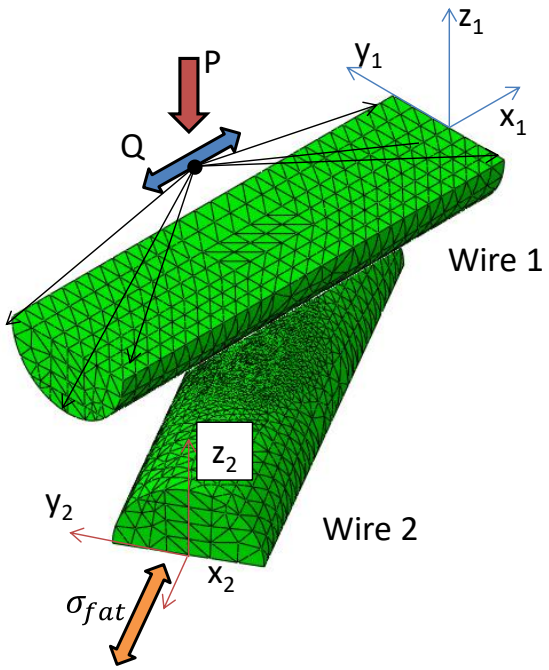

Figure 6: FE model of the contact between 2 wires with 30° of orientation, the bullet point symbolizes the reference point where loading is applied.

The mesh size in the contact region was set to 25 µm which was previously shown in [20] to be a good compromise between the stress assessment and the computation time. The aim of these simulations is also to include the cracks in the calculation in order to determine the SIFs and thus the risk of crack propagation. For this purpose, a mesh size of 10 µm was chosen for the crack front. The FEA was performed with using 4 loading steps applied to the reference point (highlighted in red in Figure 5):

Step 1 - Application of the average fatigue stress to wire #2 (X2 loading),

Step 2 - Contacting by displacement of wire 1 (Z displacement),

Step 3 - Application of normal force for contact (Z loading),

Step 4 - Application of cyclic tangential force (on X1) and fatigue stress amplitude (on X2) for 2 cycles for elasticity behavior and 5 cycles for elastoplastic behavior.

The experiments were conducted with a progressive loading until a target tangential force value was reached, then several million cycles were applied until crack initiation. Due to computational time

constraints, only 5 elastoplastic cycles are simulated. This corresponds to 5 hours of calculation with 8 CPUS. However, previous work has shown that contact stabilization is established for 10 simulated cycles, but the onset of stabilization is observed at 5 cycles [20]. For both elastic and elastoplastic simulations, the COF value applied in the fretting contact is equal to 1 which corresponds to the experimental value (figure 3).

To determine the crack arrest condition, the model must consider the crack so as to determine the amplitude of the SIFs during a cycle. This was done using the Zcracks software [27]. The used numerical method for the SIF analysis was G-θ proposed by [28] without volume force and local temperature variation [29,30]:

$$G_h = \frac{1}{S}\left[\int_\Omega \left(\sigma_{ij} u_{i,j} \theta^h_{j,k} - W\theta^h_{i,i}\right) d\Omega\right] \quad (4)$$

Where σ_{ij} is the stress tensor components, u_i is the displacement components, $u_{i,j}$ is the spatial derivative along i direction. The θ^h_j corresponds to the virtual displacement field of the crack front, where h the crack propagation mode I, II or III assessed when the virtual displacement field is respectively normal to the front, along the binormal of the front and tangential to the front. W refers to the total strain energy. In this algorithm, asymptotic values of G and K are obtained for a sufficient number of layers used in the volume integral [31]. In the present study, five layers of elements were used to evaluate G. This does not provide perfect convergence of shear modes, but the variations in shear level are small enough to keep this as a satisfactory approximation and will remain invariant throughout the study. therefore, a crack was introduced into the mesh according to the geometry and position observed in section 3.2. Thus, the crack was introduced into the finite element model at the lateral contact size with respect to this direction (X2), which corresponds to the experimental position of the crack surface. Figures 7 a) and b) show the location and orientation of the crack. The orientation is also taken from the experimental results with an angle of 30 °with respect to the surface and an angle of 15° with respect to the wire direction. Figure 7 c) displays the mesh of the

crack and the two studied points: M at the center of the of the crack front and S at the edge of the crack front.

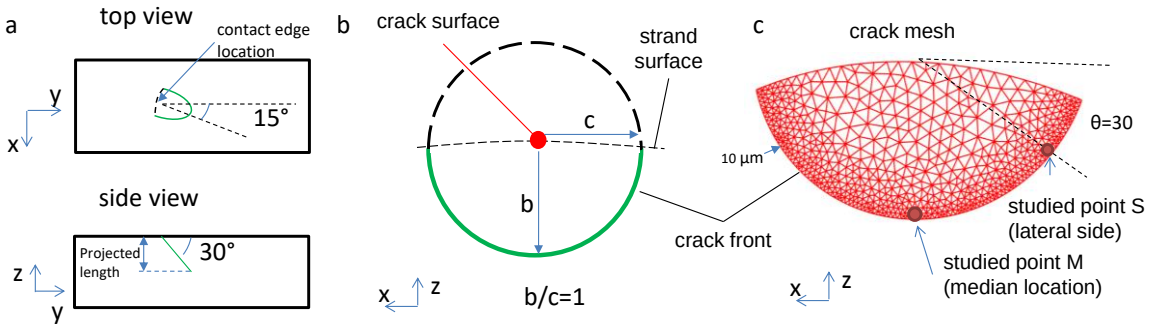

Figure 7: Definition of the modelled crack geometry a) crack location in the wire in xy and yz planes; b) location of the center of the crack in relation to the surface, in yz plane; c) mesh of the crack, in yz plane and definition of side (s) and middle (M) points of the crack front to be studied.

4.2. Elastic analysis

To reproduce the experiments (fig. 4), elastic simulations were performed for tangential forces of Q*=150 and 200 N, normal forces from P=150 N to 550 N and a fatigue stress of σ_{fat}=60 MPa with a fatigue ratio R=0.5. The COF of the crack lips, μ_{cl}, is not known but is close to the value measured in part 3.1. We decided to test this value as a parameter of the model using μ_{cl} in the range [0.5-1.3]. The aim is to evaluate the SIF at the crack front to determine the risk of crack propagation or if crack arrest is reached. Simulations were also performed with two cycles of fretting fatigue. As a first result, it was shown that the first load cycle can be considered as a transient period where the crack lips slide before reaching a stick steady state (fig. 8, i.e. the crack response then remains unchanged for the 2nd cycle). This point is observed for almost all simulated conditions (except for μ_{cl}=0.5 and P=150N). For the two load cycles, the blue part of the contact is the open part, which evolves significantly with the loads. The green part, which is the sliding part, evolves in a complementary way to the blue part. Finally, the red zone observed mainly in the median part is the stuck area of the crack face, which is not present for the Q max load and for the first cycle. However, once the steady

state related to the 2nd cycle is reached, the crack lips stick together in this region and do not slide anymore while experimentally, for this condition, the crack was still propagating. This phenomenon can be explained by the combined effect of the normal force with the crack orientation inducing a high contact pressure within the crack lips preventing the crack lips from sliding. It is worth noting that most of the lifetime data only analyze the first cycle and fails to observe this effect [2, 5].

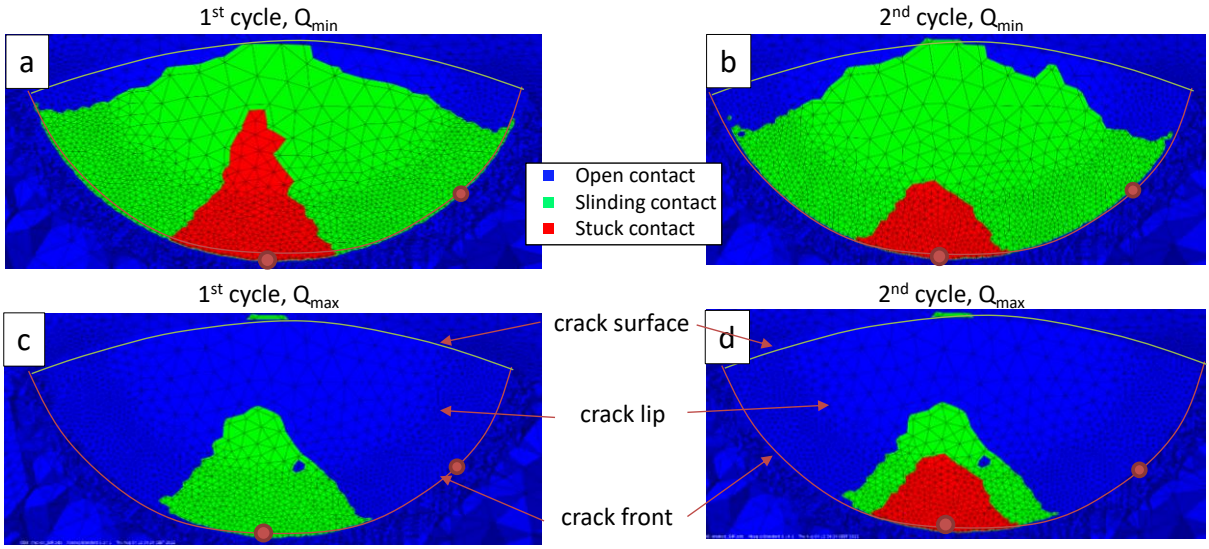

Figure 8: cracks lip contact evolution as a function of the loading and cycle for the condition Q*=150 N, P=200 N, μ_{cl}=0.5, σ_{fat}=60 MPa, Rf=0.5, b=200 µm and elastic behavior.

Again, since many literature works focus on the first load cycle to capture the SIF fluctuation in fretting fatigue crack simulation, this work proposes to consider the 2nd load cycle to reach a steady state that is more accurate and representative of the physics of the contact within a crack. Both the first and second load cycles are compared in figure 9. The SIFs on the crack fronts are plotted as a function of the loading sequence described in Figure 8. The first cycle shows an amplitude of K_I of 2.5 MPa.m$^{0.5}$ only at the edge of the crack front (see pint S), while the SIF value remains very close to zero in the median part of the crack front (see point M), figure 8(c). This suggests that the crack propagation, at least for the central part of the crack, depends mainly on the shear modes. A significant evolution of K_{II} and K_{III} is observed on the throughout front. For the second cycle, which is more representative of the real situation, the K_I shows an amplitude similar to that of the first cycle. On the other hand, the K_{II} and K_{III} amplitudes do not evolve in the central zone, which corresponds to

the stuck zone. This result is a direct consequence of the bonded state of the crack lips achieved just after the first loading cycle. In fact the amplitude of the SIFs converges to zero.

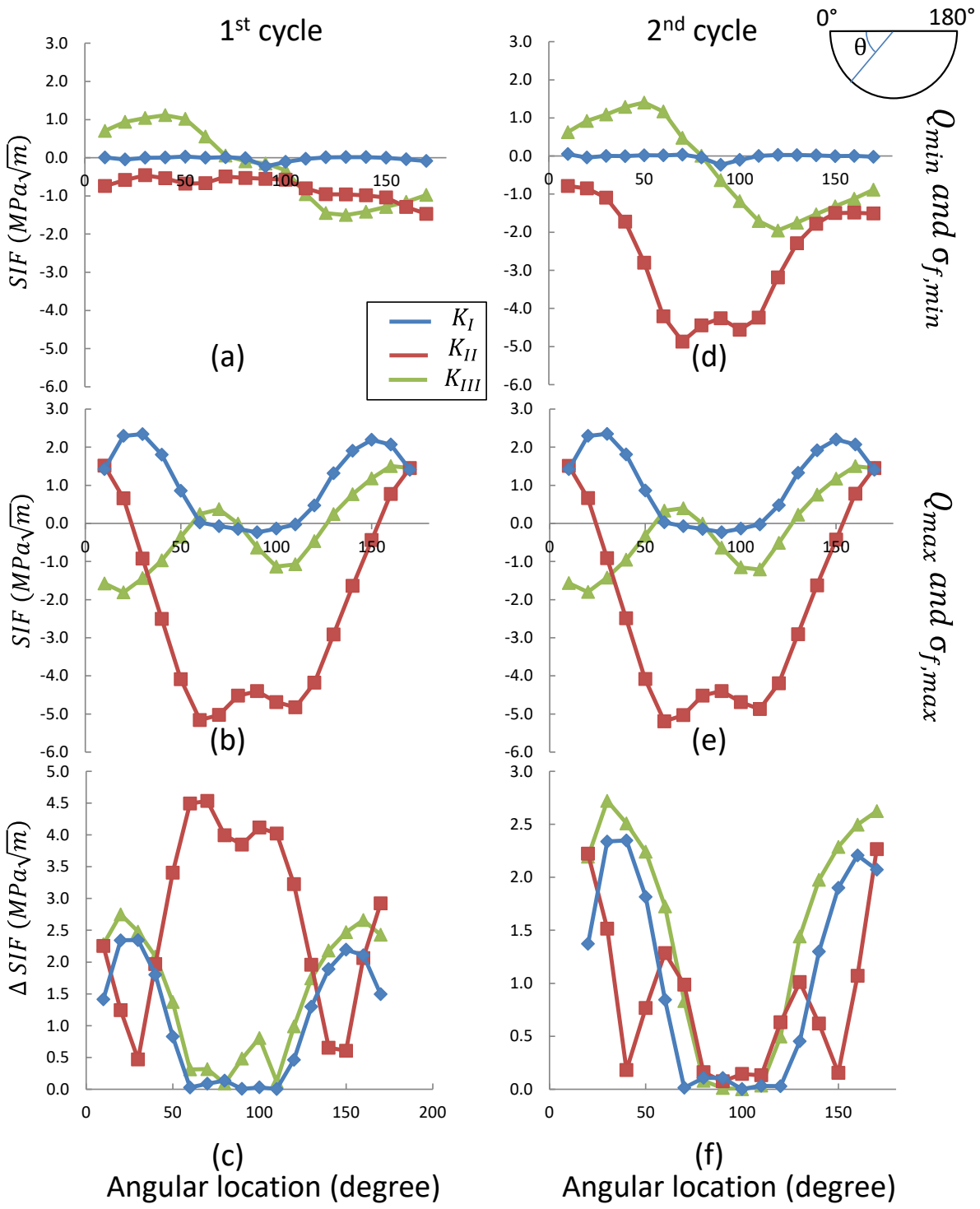

Figure 9: SIF for the condition Q*=150 N, P=200 N, Q*=0.5 σ_{fat}=60 MPa, Rf=0.5 b=200µm and elastic behavior; for the first cycle a) at Q_{min} and σ_{min}; b) at Q_{max} and σ_{max}; c) the SIF amplitude; and for the second cycle d) at Q_{min} and σ_{min}; d) at Q_{max} and σ_{max} e) the SIF amplitude.

A conclusion of this investigation is that an analysis considering only the first load cycle tends to overestimate the mode II contribution leading to a misinterpretation of the cracking process in fretting fatigue as it relates only to a numerical transient situation. The second cycle appears to be more representative to capture the steady state situation and provides significantly lower ΔK_{II} value. The analysis is now restricted to 2nd loading cycle. The elastic model suggests a significant crack lip sticking zone which is inconsistent with the experimental crack extension. Therefore, it is not possible to correlate the evolution of the SIF as a function of normal force with the experimentally observed crack arrest extension in the central part of the crack front.

Furthermore, figure 10 underlines that ΔK_{II} becomes almost equal to zero, except for the COF 0.5 and for P=150 N. Based on these results, the computed ΔK_{II} values cannot explain the experimental crack arrest threshold values observed at $P_{CA\ (Q^*=150)}$=300 N and $P_{CA\ (Q^*=200)}$=450 N. This again confirms that the given elastic analysis is not representative of the experimental condition and cyclic plasticity must to be considered in the model.

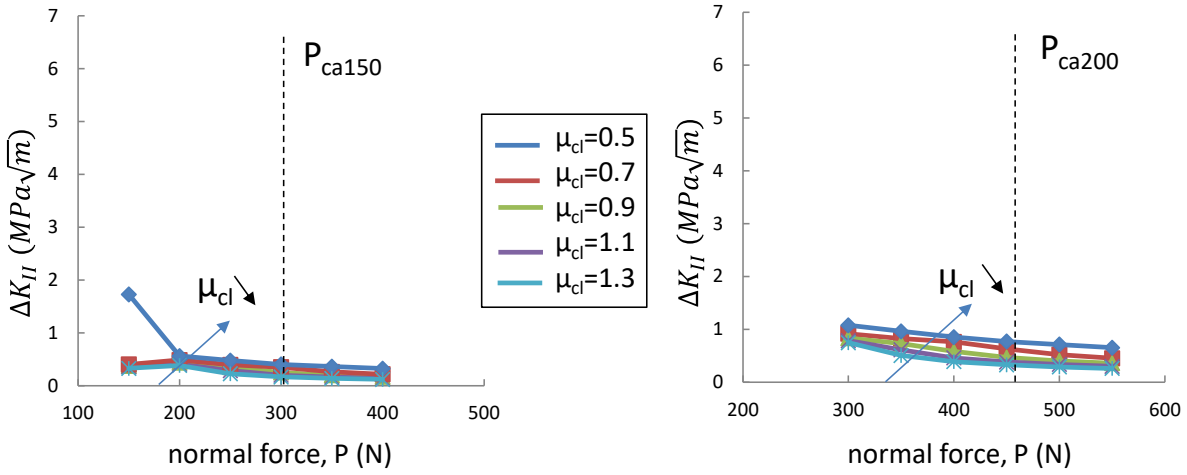

Figure 10: SIF amplitude evolution in mode II, $\Delta K_{II,}$ as a function of normal force for different values of COF between crack lips, elastic model and for the 2nd cycle.

4.3. Elasto-plastic analysis

4.3.1. mechanical analysis of the crack

Elastoplastic simulations were carried out for the same conditions as for the elastic analysis with Q*=150 and 200 N and normal forces from 200 N to 500 N. Again, since the COF between the crack lips is unknown, this value was considered as a parameter of our FEA varying from 0.5 to 1.3. Figure 11 shows the contact conditions of the crack lips at conditions Q*=150 N with forces P=250 and 300 N as a function of the COF: for the 5^{th} cycle and at the maximum load level, namely P_{max} and σ_{max}. It is recalled that the normal force to stop cracking for Q*=150 N is P_{CA}=300 N. On the other end, the P=300 N - Q*=150 N numerical computation is simulating a crack arrest situation. It is interesting to note that contrary to the elastic analysis, the interface remains in a sliding condition for COFs up to 0.9 for 300 N and 1.3 for 250 N normal force. These COF values correspond approximately to the COFs found experimentally using fretting sliding tests (section 3.1). These results appear to be in better agreement with the experiment. In fact, the FEA yields a sticking interface for values of both normal force and COF values that are closed to the experimental values. Nevertheless, due to the high plastic deformation, the contact within the interface is complex to model in terms of convergence: some nodes remain in the open state in the center of the contact area within the crack lips, despite the authors' attempts to optimize contact parameters to achieve numerical convergence; however, these efforts did not yield the desired improvement in the results. This point is considered to be a numerical artifact and should not affect the above conclusion: the plastic model modifies the contact condition to a large extent as compared to the elastic model assumption.

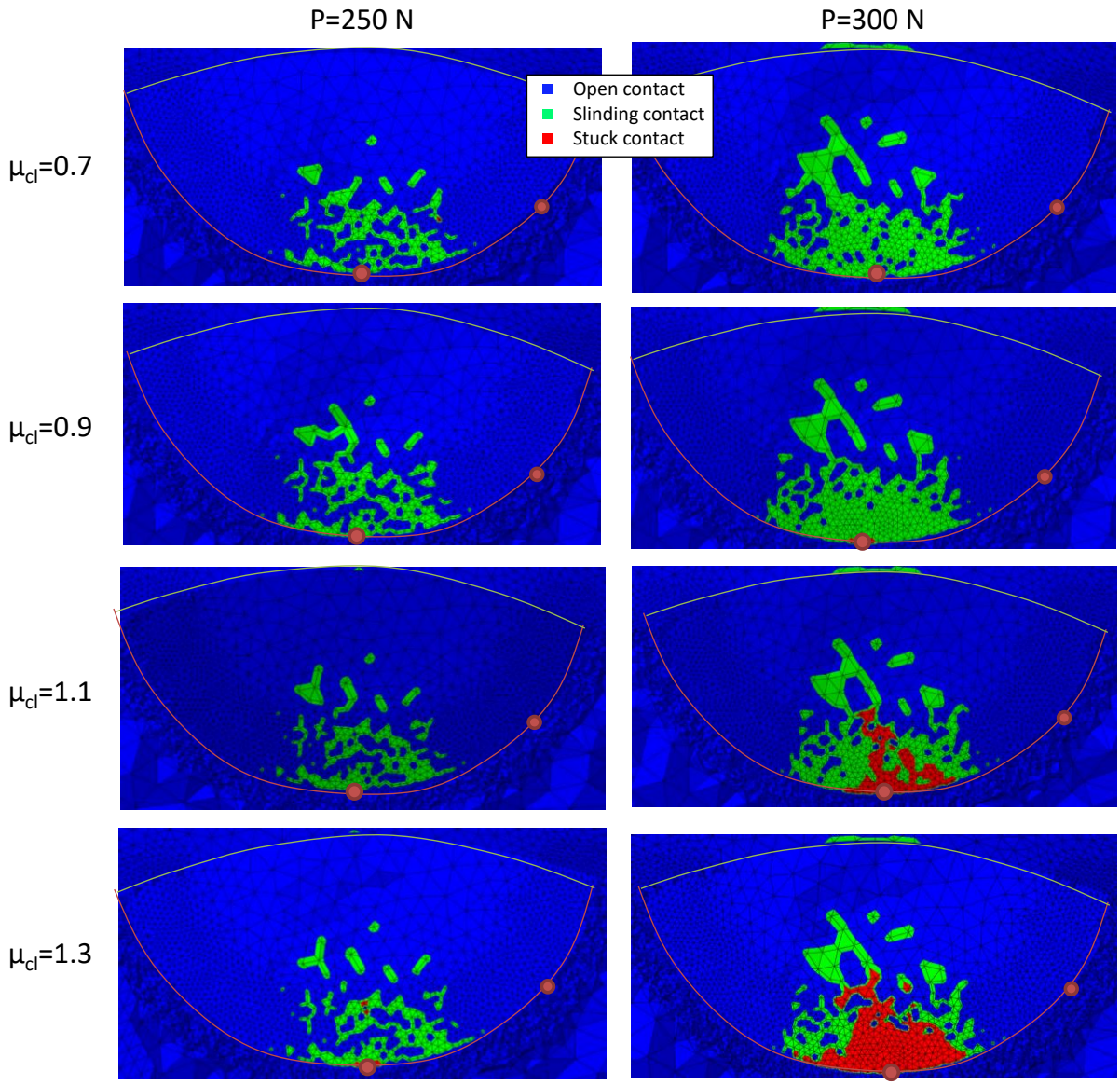

Figure 11: sliding condition in crack lips for Q*=150 N, P=250 and 300 N, σ_{fat}=60 MPa and R=0.5 in function of the COF.

To better understand the evolution of the contact during a cycle figure 12 shows the crack lip contact pressure at specific locations on the crack surface for P=200 N Q*= 150 N and μ=0.9 loading condition. For the first location close to the central part of the crack front (M point), the crack lips pressure displays a large fluctuation from 100 to 360 MPa. The second location, close to the lateral crack front at a 30° angle (S point), displays a pressure varying from 0 to 40 MPa. The third location is in the middle of the crack lips and the evolution is from 25 to 310 MPa. The pressure evolution is in phase with the fretting fatigue loading and unloading of the crack lips. Along the median location, the crack is always closed and the pressure has reached a high value whereas the middle part of the

crack lip opens and closes, for lower pressure values. Thus, the contact conditions are very variable depending on the location on the crack surface. These conditions can affect the frictional response. When the average contact pressures of part 3.1. are analyzed, they appear to be very close to each other, about 80 MPa (normal load divided by final contact area). It is therefore very complex to correlate these fretting friction values with the pressure sliding conditions operating between the crack lips. In addition, the reported friction tests may depend on the contact size increase induced by wear and plastic deformation. Note that the wear perturbations do not occur within the crack lips. However, very small fluctuation of the coefficient of friction is observed depending on the normal force during the friction test. Hence, a quasi-constant friction value can be assumed over the whole crack lip surface whatever the local pressure situation.

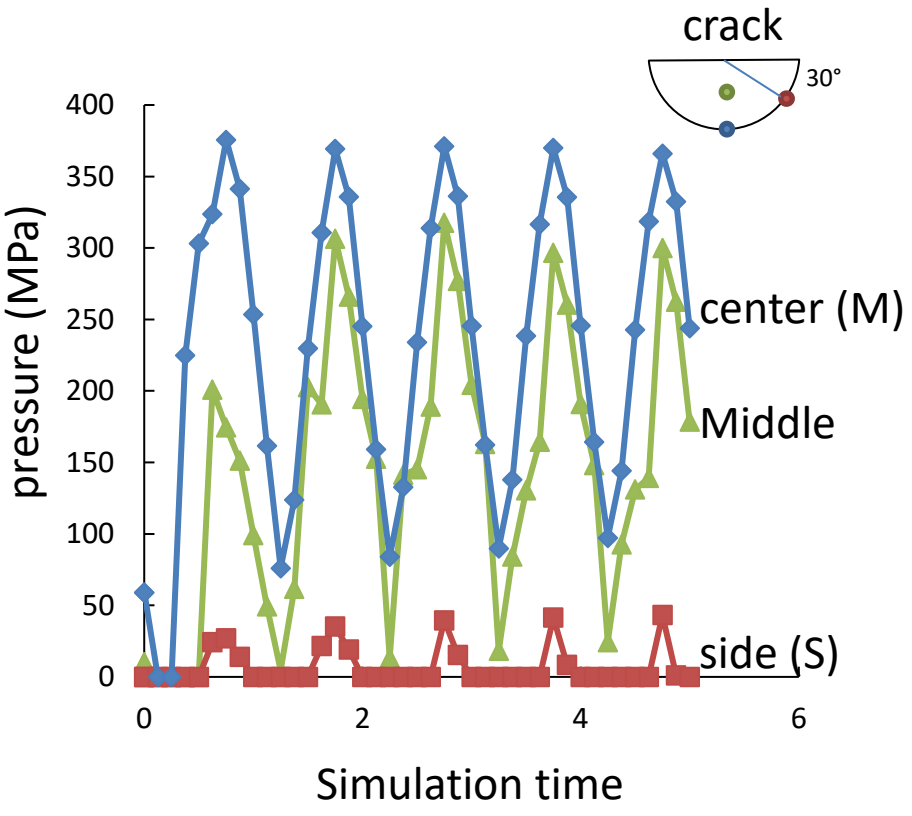

Figure 12: pressure at center side position of crack front and middle position of crack lips as function of simulated time for the following conditions: P=200 N Q*=150 N μ=0.9; σ_{fat}=60 MPa b=200 μm.

Therefore, assuming a constant friction value μ_{cl}=0.9 over the whole crack surface, the evolution of the FICs at the crack surface for P=250N and Q*=150N at the 5th cycle and for EP simulation are plotted in figure 13. While the mode I remains quite similar to the elastic case, a clear fluctuation of the mode II contribution is observed. For mode II, the SIF value is close to zero at the centre of the crack front for Q_{min} and σ_{min} and increases in absolute value for Q_{max} and σ_{max}. Hence the SIF amplitude in mode II increases to 1 MPa.m$^{0.5}$ at the point M. Mode III exhibits two profiles that are almost equivalent for the maximum and minimum loading conditions leading a lower amplitude less than 0.5 MPa.m$^{0.5}$.

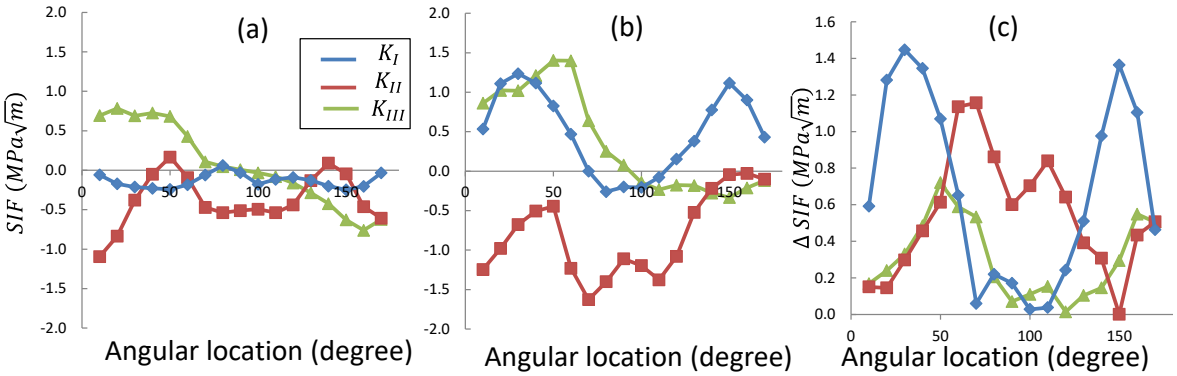

Figure 13: SIF for the condition Q*=150 N, P=200 N, μ_{cl}=0.9 σ_{fat}=60 MPa, R=0.5 b=200µm and elastoplastic behavior for the 5th cycle; a) at Q_{min} and σ_{min}; b) at Q_{max} and σ_{max}; c) ΔK profile.

These results show the importance of mode II in the propagation of the studied cracks especially in median part of the crack front (M point). In fact, due to the high shear stresses, the crack has a 30° orientation under the contact, and seems to propagate in mode II over a distance of at least 200 µm experimentally. Mode III with plasticity tends to stabilize its value and can therefore be neglected. Conversely at the side of the crack front, the crack propagation appears to be driven mainly by a mixed loading process (modes I and II).

Figure 14 shows the evolution of the SIF in mode II as a function of the SIF in mode I during the 5th cycle, considering both M and S points. At the M points, we observe only cyclic evolution of mode II, where the crack remains closed during most of the cycle, while the SIF values in mode I mostly negative and constant (figure 13). Once again mode II is the main driving force for cracking at M

points (i.e. median axis). The behavior of the selected lateral point shows a large hysteresis and a non-proportional load path compared to the central location: the crack remains open for most of the cycle, with mode I SIF reaching positive values (figure 13). However, the SIF values in mode I are limited considering the threshold amplitude values for mode I, which is about 2 MPa.m$^{0.5}$ [32-35]. Thus, it appears that at the contact edge (S point), modal mixing plays an important role in crack propagation.

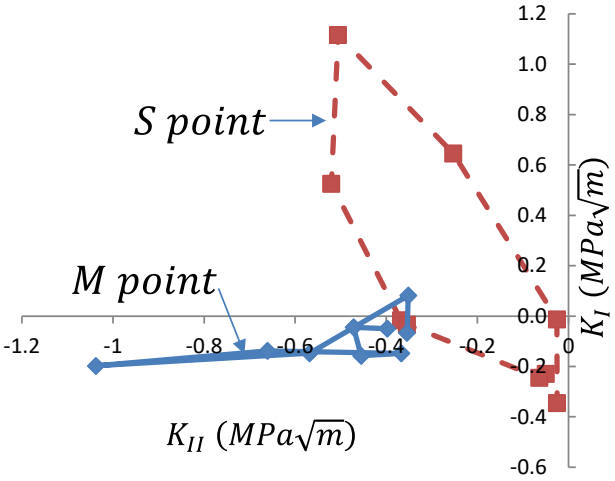

Figure 14: K_{II} as a function of K_I at for M and S points at the 5th cycle.

Last but not least, the point of plastic intensity should be addressed. Within the contact between the two strands, the plastic level clearly corresponds to large scale yielding condition. However, the obtained SIF amplitudes question the level of plasticity associated with the crack tip. In the above results, cyclic plastic radius is observed to be limited to 0.2 mm, which is consistent with these very low levels of SIF amplitude. In this respect, the SIF analysis is consistent with the confined plasticity assumption made for numerical analysis of fatigue cracks using the G–θ method.

4.3.2. influence of crack geometry on the SIF

Knowing the length and the location of the cracks in the contact is paramount for accurate assessment of SIF in fretting fatigue. These two parameters can play an important role in the stress distribution around the crack front and the subsequent SIF values. Therefore, this section presents the effects of varying these geometric parameters on the SIF values analyzed at the middle and at the lateral side of the crack front, the so-called M and S points respectively.

In the given investigation we have chosen to locate the crack at the contact border where the application of a multiaxial fatigue criterion predicts the maximum cracking risk. This location of the propagating cracks is indeed widely considered in the literature [6, 10]. However, at the contact opening, it is sometimes mentioned that the cracks are slightly offset inside the sliding zone. Lamethe et al. [36] through the study of various co-polymers and the use of a spherical transparent glass counter body have clearly shown that crack nucleation is exactly located at the contact border along the median loading axis. However, as the cracks grow, they note a decrease in contact stiffness which subsequently induces an expansion of the contact area. Thus, at the contact opening, the cracks seem to appear within the sliding interface whereas initially they were well located at the contact borders. The analysis of the SIF variations for the given crossed wire aluminum contact confirms these conclusions. In fact, if we compare the evolution of the SIF by positioning a crack slightly inside the contact (-200 µm) (Fig. 15) we notice that the SIF values found along the median axis (point M) and in particular the ΔK_{II} component at the M point are extremely low and are totally incompatible with the observed propagation process. On the other hand, the analysis at the contact edge (0 µm) confirms that the ΔK_{II} value is sufficiently high to allow propagation. On the side of the crack front (S point), the ΔK_{II} is low. The other two amplitudes show inverse phenomena, low at the center and high at the sides. Thus, through this simple analysis of the SIF evolution in terms of crack expertise, we confirm the hypothesis that propagating cracks are well initially localized at the contact edges. The postmortem observation of internal cracks in the sliding zone is, as suggested by Lamethe et al., an artifact induced by the crack extension which reduces the contact stiffness induces a contact area extension and the a posteriori shift of the apparent contact edge. To complete the

analysis, some simulations were carried out assuming a crack location outside the contact area (+200 µm). Surprisingly, the calculated SIF ranges are quite high and could favour significant crack propagation. However, both surface examinations and crack nucleation simulations never confirm the occurrence of fretting fatigue cracks outside a fretting scar. Therefore, this external crack location hypothesis is not realistic and cannot be considered.In the remainder, the cracking site will be systematically positioned at the computed contact edge.

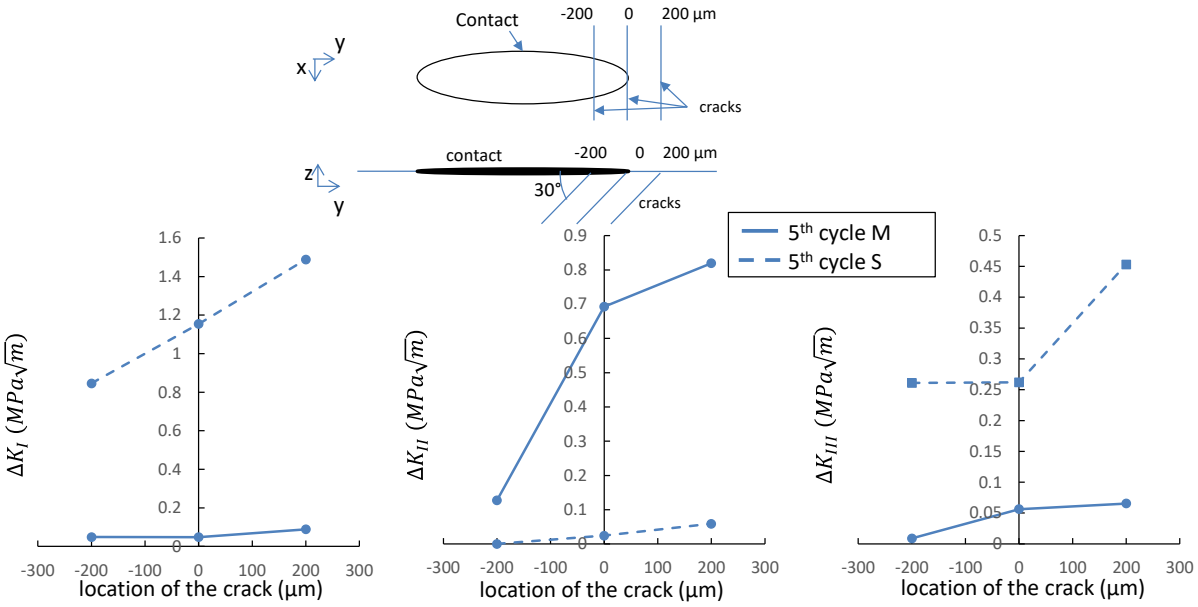

Figure 15: evolution of ΔK values for each of the three modes, as a function of the crack location relatively to the edge of the crack: 0 is the edge of the contact edge, negative (reps. positive) values are within (resp. out of) the contact area. Points M and S are analyzed (5th cycles for conditions P=250 N, Q*=150 N, µ=1; σ_{fat}=60 MPa b=200 µm).

Although the crack could be semi-elliptical, above analyses in the paper were carried out using a semi-circular crack: experimentally the shape of the crack seems to correspond to an ellipse for which the width is larger than the depth of the crack. The length to width ratio is of about b/c=0.3 but remains complex to assess.

Figure 16 shows the evolution of ΔK for the 5th cycles at points M and S on the crack front as a function of the radius perpendicular to the contact direction. Overall, the ΔK values increase with crack width for b value varying from 200 to 400 µm. For mode I, if the crack is not wide enough, the amplitude is zero because the geometry does not allow the crack to open and slide. Conversely, increasing its width increases the SIF amplitude at the edges but the SIF values remain very low in the center of the crack front. For mode II, an increase is observed between 200 and 400 µm, which is explained by the decrease in stiffness due to the widening of the crack, it seems that when the crack reaches a semicircular shape, for width of about 400 µm, the ΔK_{II} value tend to reach a local maximum. Mode III increases, but remains negligible for the M point, while it could play a role for the point S. Thus, these simulations suggest that the results for the center part of the front is similar for elliptical (b>400µm) and semicircular crack (b=400 µm) shapes but evolve at the side part.

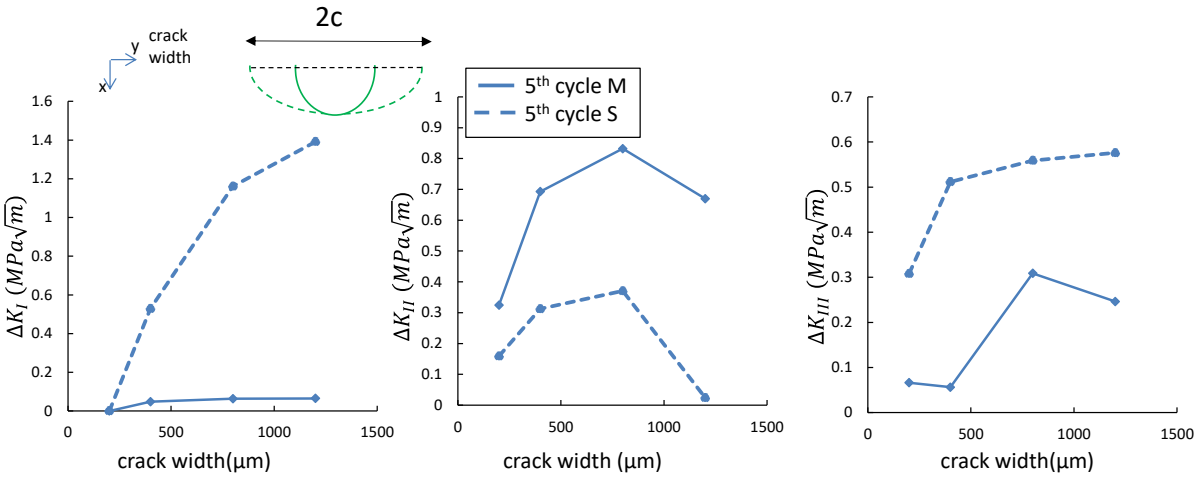

Figure 16: evolution of the amplitude of ΔK as a function of the crack width for the 5th cycles and for the center and the side of the crack front; condition P=250 N Q*=150 N µ=1; σ_{fat}=60 MPa b=200 µm.

The last parameter to be tested is the size or the radius of the semi-circular crack which is equal to the projected length of the crack as detailed in figure 17. All SIF values are again detailed as amplitude for the 5th cycle. For ΔKI, at the M point of the crack front, the value first decreases and increases for longer crack; meanwhile, for ΔKII values a monotonic decrease is observed. This

observation can be related to the experimental observations where at the crack nucleation, the crack is orientated at 30° and then for long cracks (>200 µm) the crack deviates to 90°, orthogonally to the fatigue load [10]. The interpretation is that the crack is driven by mode II up to ~200 µm. If the normal load on the contact is not too high, the crack can grow sufficiently to reach an area where the mode I can be activated, at which point the crack will deviate and propagate up to failure. Otherwise, the crack is in crack arrest mode due to normal force and there is no failure until 10^7 cycles. The mode III decreases with the size of the crack but seems important in the early stage of the crack even for the mid point M.

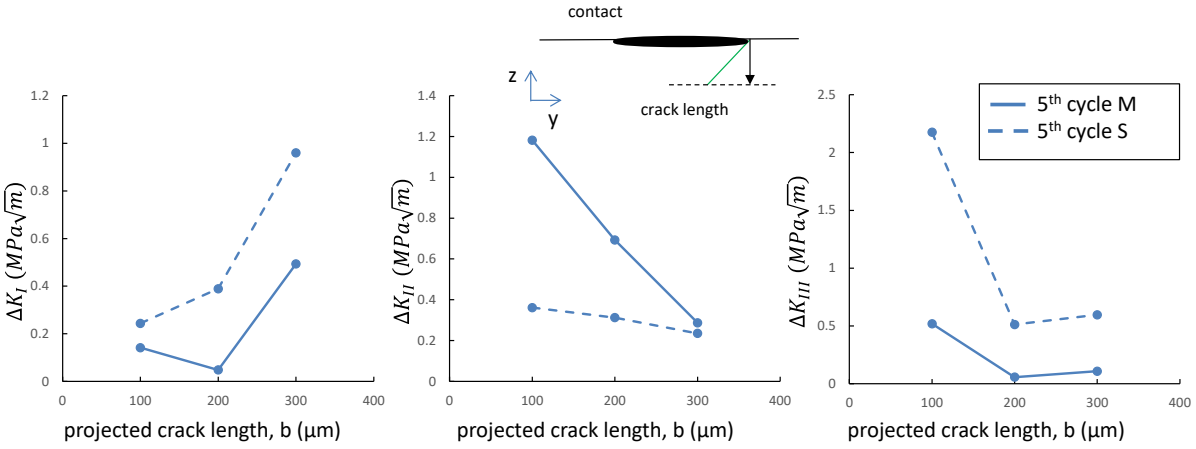

Figure 17: evolution of the amplitude of ΔK as a function of the projected crack length for the 5th cycles and for the center and the side of the crack front; condition P=250 N Q*=150 N µ=1; σ_{fat}=60 MPa.

Finally, from the above analysis, it can be concluded that the location of the crack is at the edge the contact so as to maximize SIF amplitudes values. The width of the crack increases mainly the mode I but only at the side location. The variation in crack size explains that beyond 200 µm of projected length, the crack is first mainly driven by mode II then by mode I for long crack. If the crack is not long enough to be loaded in mode I, crack arrest occurs, otherwise mode I is activated and the strand breaks when additional fatigue stress is applied which corresponds to the experimental observation.

4.3.3. influence of the friction on the SIF

The COF between the crack lips is a key aspect of crack propagation within the scope of fretting fatigue. To understand the effect of friction coefficient, the slip amplitude of the crack lips was extracted from the FEM simulations. Figure 18 shows the friction cycles corresponding to a tangential force Q*=150 N taken from a node of the crack lip near the center of the crack front for different normal force and coefficient of friction. Despite the limited number of points to describe the friction cycles, it is possible to extract the slip amplitude. The latter is directly influenced by the normal force and the friction coefficient of the crack lips. First, for high COF values or high normal forces, the friction cycles are closed and there is no slip. Secondly, the sliding amplitude appears to be inversely proportional to the COF and the normal force. It can be observed that the slip amplitude is about ~58 nm for a COF of 0.5 and drops to ~10 nm for a COF of 0.9 and to zero for a COF of 1.3.

An interesting parameter is the calculated cumulative sliding. In the literature, this phenomenon is usually found in assemblies [37]. This cumulative sliding is possible due to the cumulative plastic strain around the crack. Based on the orientation of the contact and the associated frictional forces, plastic strain occurs preferentially in a unidirectional manner, facilitating sliding in this same direction. Thus, plastic simulations of fretting fatigue conditions allow to find representative values of the SIF which can be found thanks to this accumulation of plasticity that allows sliding between the crack lips. These results suggest that the unidirectional plastic strain is a key factor in controlling the frictional sliding in the crack lips and the load at the crack front. It is worth noting that this displacement of the crack lips is of the same order of magnitude as the crack propagation increment. These two phenomena can interact and influence the SIF values.

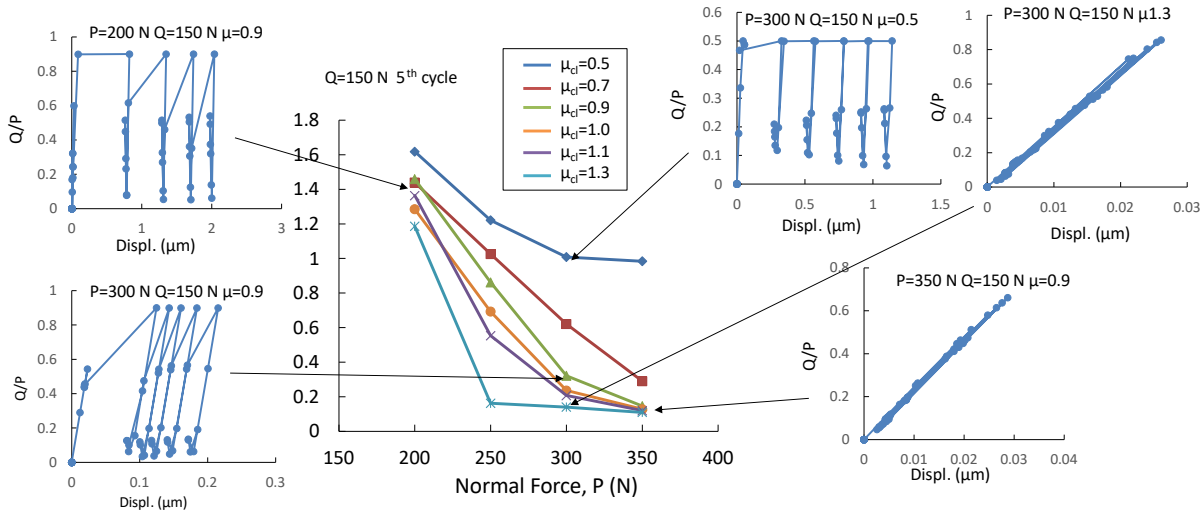

Figure 18: analysis of the sliding displacement in crack lips as function of COF and normal force for Q*=150 N and without fatigue loading.

5. reverse identification of the friction coefficient between crack lips

As demonstrated by the above results, the COF between the crack lips has a strong influence specially on the SIF II. Then it is important to well evaluate this parameter in order to be able to predict the lifetime. However, to evaluate this value in fretting fatigue, DIC methods [19] aren't possible, hence, we propose to correlate the evolution of the ΔK_I and ΔK_{II} with the experimental normal force threshold P_{CA} marking a crack arrest process.

A campaign of simulations had been performed to simulate the evolution of ΔK_I and ΔK_{II} amplitudes as a function of the normal force and the coefficient of friction along the median axis (θ=90°) at the 5^{th} load cycle for Q*=150 N and Q*=200 N, taking the previous results into account: semicircular crack shape, length of 200 µm and crack location at the edge of the contact.

For the mode I, it is interesting to note that the ΔK_I values remain very small (<1 MPa.$m^{0.5}$) when considering the loading conditions (i.e. P<200 N, Q*=150 N, µ>0.3). This suggests that the mode I contribution can be neglected in the propagation process along the median axis. The ΔK_{II} exhibits different evolution: the values are initially small and increase with the number of load cycles,

independent of the tangential force. Again, there is an inverse proportionality of ΔK_{II} values as a function of friction and normal forces. However, since the ΔK_{II} values are higher than for the ΔK_{I} values, it can be concluded that the mode II is the driving force for crack propagation.

By combining these results with experimental conditions of crack arrest, it is possible to propose a method for determining the apparent COF between the crack lips. This analysis consists in assuming that the crack arrest is reached when ΔK_{II} is below a threshold value for instance $\Delta K_{II,th}$ =0.6 MPa.m$^{0.5}$ according to which ΔK_{I} is negligible (ΔK_{I}<0.1 MPa.m$^{0.5}$) such that : ΔK_{II}< $\Delta K_{II,th}$=0.6 MPa.m$^{0.5}$ and ΔK_{I}< $\Delta K_{I,th}$=2 MPa.m$^{0.5}$.

Then the evolution of ΔK_{I} and ΔK_{II} versus the applied normal force P is compared for varying μ_{cl}, figures 19 and 20. These different simulations underline a very good correlation with the threshold normal force loading to crack arrest situation $P_{CA(Q^*=150)}$=300 N or $P_{CA(Q^*=200)}$=450 N according to the fact that the COF between the crack lips is adjusted around μ_{cl}=0.9. Thus, using the reverse analysis of the plain fretting crack arrest situation, a representative crack lips friction coefficient μ_{cl}=0.9 is derived.

Furthermore, this COF is very close to the energetic COF determined from the variable fretting sliding test (part 3.1). This suggests that simple fretting friction tests could be considered to estimate the friction coefficient operating within sliding crack lips. This COF is representative of the initial sliding of the crack lips and therefore has a direct effect on the stress at the crack front due to shear loading. It therefore allows crack arrest to be characterized by Mode II loading dependent on crack lip sliding, which in the 3D case of fretting fatigue cannot be measured directly by DIC [19]. Nevertheless, the characterized COF of the crack lips, even if its value is close to that observed experimentally, is also an apparent COF. In fact, crack lips can be rough and should induce a non-coulombic friction similar to mechanical inking and plowing [38]. However, in our case the effect seems to be almost negligible. A final remark can be made about the values of the amplitude ΔK_{II} for the case where the crack lips are not sliding. These values should be zero because the shear is completely absorbed by the friction

of the crack lips. In reality, it should be noted that the FEM simulations carried out with Abaqus cannot take into account the sliding on the crack front element, so the deformation of the last element transmits a force to the crack front, which leaves a residual SIF amplitude.

This methodology can also be used to find the $\Delta K_{II,th}$ if the crack lip friction coefficient is known. In our case, our crack arresting properties are low, which has enabled us to approximate our threshold, but if the latter has a large value, the threshold will not be found at the inflection of the ΔK_{II} curve as a function of normal force. In the same way, therefore, it is possible to match the simulated ΔK_{II} to the experimental crack arrest as a function of normal force, and thus determine an approximation of the mode II crack arrest threshold.

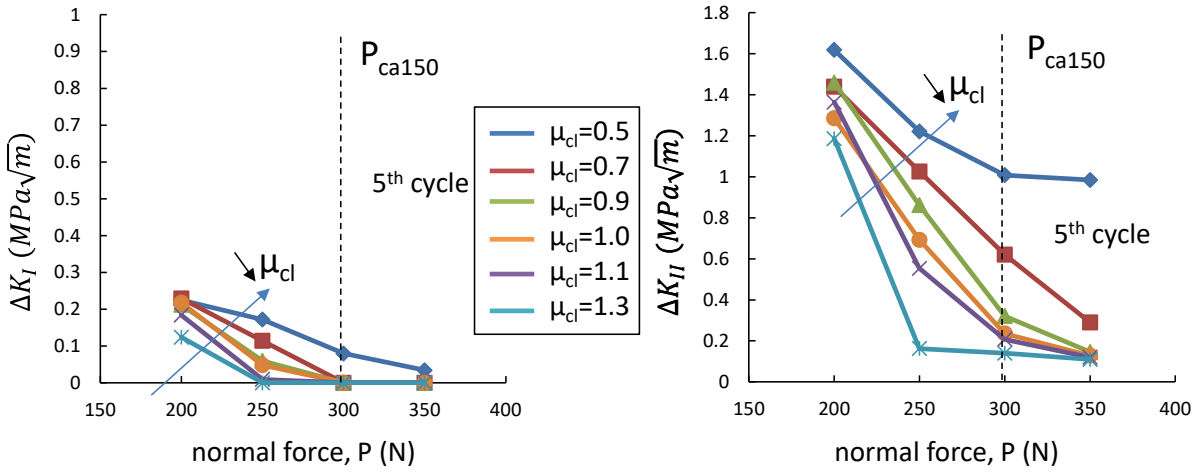

Figure 19: SIF at the M point for Q*=150 N as function of the normal force and COF of the crack lip at the 5th cycles

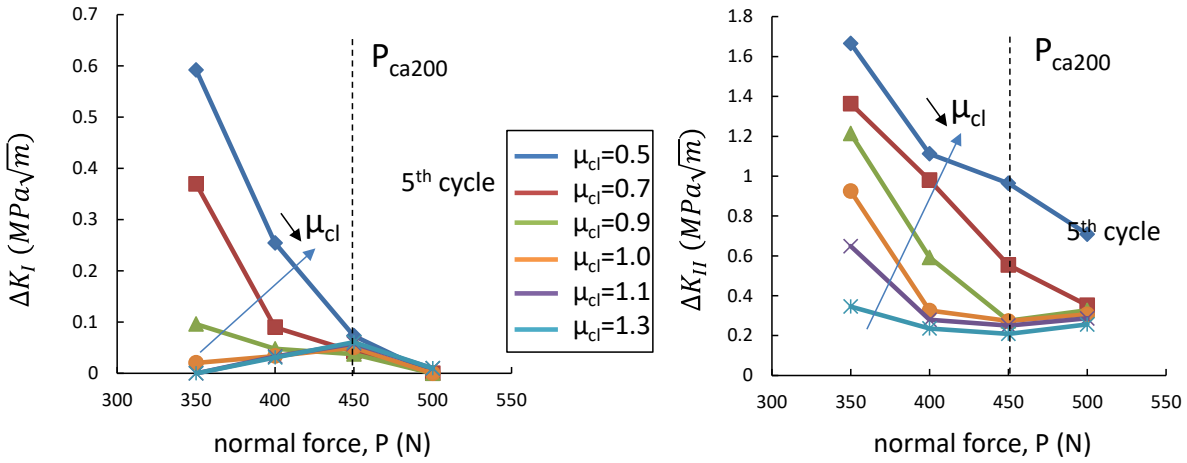

figure 20: SIF at the M point for Q*=200 N as function of the normal force and COF of the crack lip at the 5th cycles

Conclusion

The aim of this combined study was to analyze the experimental fretting fatigue cracking process through both elastic and elastoplastic simulations, with a focus on understanding crack arrest phenomena induced by complex multiaxial loading.

- Fretting fatigue experiments highlighted the threshold normal force inducing crack arrest in plastic crossed aluminum wire contacts.
- Experimental friction characterization tests were conducted at different normal forces to characterize the coefficient of friction (COF) in aluminum/aluminum contacts. The measured COF, influenced by high plastic strain, was deemed overestimated, leading to the use of the energetic COF in the analysis.
- Simulations employing elastic properties failed to capture crack propagation under various conditions, regardless of the COF value in the crack lips (μ_{cl}). Elastic simulations consistently indicated that the crack lips were stuck (no sliding), making them inadequate for assessing the experimentally observed risk of crack propagation.
- Examination of crack geometry revealed that the ellipticity of the crack give a quasi constant value of ΔK_{II} at the middle of the crack front but increases the amplitude of the three modes

at the side. Cracks were observed at the edge of the contact, in line with classical experimental observations.

- Stress Intensity Factor (SIF) analysis demonstrated an evolution of ΔK in line with experimental observations. ΔK_I was of low value the contact and increased after 200 µm, while ΔK_{II} showed an initial significance that decreased around 200 µm. Notably, the crack, initially oriented at 30°, bifurcated around 200 µm to align orthogonally with the fatigue stress.
- Elastoplastic simulations were found to be crucial for modeling crack propagation, with the COF of the crack lip identified as a key factor.
- A method is proposed to determine the apparent COF in the crack lips by modelling crack arrest by normal force. Using a post-processing analysis of crack arrest fretting tests, it is possible to extrapolate a representative coefficient of friction operating within the sliding crack lips (presently μ_{cl}=0.9). The value obtained is consistent with the friction value derived from plain fretting sliding experiments. Therefore, this investigation also suggests that adequate fretting sliding tests could be used to extrapolate the unknown coefficient of friction operating within crack lips undergoing Mode II propagation.
-

In conclusion, this integrated research underscores the necessity of employing elastoplastic simulations for a comprehensive understanding of the fretting fatigue crack propagation process under complex multiaxial loading conditions.

References

[1] Waterhouse RB, Fretting Fatigue Applied Science Publishers; 1981

[2] Said J, Garcin S, Fouvry S, Cailletaud G, Yang C, Hafid F, A multi-scale strategy to predict fretting-fatigue endurance of overhead conductors, Tribol Int 143 (2020) 106053.

[3] Kalombo RB, Araújo JA, Ferreira JLA, da Silva CRM, Alencar R, Capra AR, Assessment of the fatigue failure of an all aluminum alloy cable (AAAC) for a 230 kV transmission line in the Center-West of Brazil, Eng. Fail. Anal. 61 (2016) 77–87.

[4] Lalonde S, Guilbault R, Langlois S, Numerical analysis of ACSR conductor-clamp systems undergoing wind-induced cyclic loads, IEEE Trans. Power Deliv. 33 (2018) 1518–26.

[5] Rocha PHC, Langlois S, Lalonde S, Araújo JA, Castro FC, A general life estimation method for overhead conductors based on fretting fatigue behavior of wires, Theoretical and Applied Fracture Mechanics 121 (2022) 103443.

[6] Araújo JA, Castro FC, Matos IM, Cardoso RA, Life prediction in multiaxial high cycle fretting fatigue, Int. J. Fatigue 134, (2020) 105504.

[7] Matos IM, Rocha PHC, Kalombo RB, Veloso LACM, Araújo JA, Castro FC, Fretting fatigue of 6201 aluminum alloy wires of overhead conductors, Int. J. Fatigue vol. 141 (2020) 105884.

[8] Matos IM, Araújo JA, Castro FC, Fretting fatigue performance and life prediction of 1120 aluminum alloy wires of overhead conductors, Theor. Appl. Fract. Mech. vol. 121 (2022) 103521.

[9] Garcia MA, Mendes Veloso LA, Castro FC, Araújo JA, Ferreira JLA, Moreira da Silva CR, Experimental device for fretting fatigue tests in 6201 aluminum alloy wires from overhead conductors, Wear 460–461 (2020) 203448.

[10] Said J, Fouvry S, Cailletaud G, Basseville S, Coulangeon M, Brocard J, Yang C, Hafid F, A global–local approach to predict the fretting-fatigue failure of clamped aluminum powerline conductors: From mono-contact crossed wires to full conductor vibrational tests, Engineering Failure Analysis 146 (2023) 107073.

[11] Said J, Fouvry S, Cailletaud G, Yang C, Hafid F, Shear driven crack arrest investigation under compressive state: Prediction of fretting fatigue failure of aluminium strands, International Journal of Fatigue 136 (2020) 105589.

[12] Zaid M, Bonnand V, Doquet V, Chiaruttini V, Pacou D, Depouhon P, Fatigue crack growth in bearing steel under cyclic mode II+ static biaxial compression, International Journal of Fatigue 163 (2022) 107074.

[13] Maurel V, Chiaruttini V, Abecassis M, Koster A, Dezecot S, Influence of a 3D realistic crack path in the driving forces for fatigue crack growth under mode I+II loading, Theoretical and Applied Fracture Mechanics 108 (2020) 102570.

[14] Ribeaucourt R, Baietto-Dubourg M-C, Gravouil A, A new fatigue frictional contact, crack propagation model with the coupled X-FEM/LATIN method, Computer Methods in, Applied Mechanics and Engineering 196(33-34), 2007, 3230-3247.

[15] Maurel V, Chiaruttini V, Köster A, Missoum-Benziane D, Fatigue crack growth under large scale yielding condition: a tool based on explicit crack growth, Journal of Theoretical, Computational and Applied Mechanics, 2023, https://doi.org/10.46298/jtcam.9296

[16] Rao KBS, Schiffers H, Schuster H, Nickel H, Influence of time and temperature dependent processes on strain controlled low cycle fatigue behavior of alloy 617, Metallurgical Transactions A 19(2) (1988) 359-371.

[17] Fessler E, Andrieu E, Bonnand V, Chiaruttini V, Pierret S, Relation between crack growth behaviour and crack front morphology under hold-time conditions in DA Inconel 718, International Journal of Fatigue 96 (2017) 17-27.

[18] Bonniot T, Doquet V, Mai SH, Mixed mode II and III fatigue crack growth in a rail steel, International Journal of Fatigue 115 (2018) 42–52.

[19] Bonniot T, Doquet V, Mai SH, Fatigue crack growth under non-proportional mixed-mode I + II. Role of compression while shearing, International Journal of Fatigue 134 (2020) 105513.

[20] Arnaud P, Maurel V, Fouvry S, Said J, Yang C, Hafid F, Fretting tests for cyclic plastic law identification: Application to a 1XXX aluminium crossed wire contact, Tribology International 177 (2023) 107958.

[21] Koprowski P, Bieda M, Boczkal S, Jarzębska A, Ostachowski P, Kawałko J, Czeppe T, Maziarz W, Łagoda M, Sztwiertnia K. AA6013 aluminum alloy deformed by forward-backward rotating die (KoBo): microstructure and mechanical properties control by changing the die oscillation frequency. J Mater Process Technol 253 (2018) 34–42.

[22] Ma X, Chen J, Yang Y, Li L, Chen Z, Yan W. Temperature dependence of microstructure and texture in cold drawn aluminum wire. Trans Nonferrous Met Soc China 27 (2017) 763–70.

[23] Besson J, Cailletaud G, Chaboche JL, Forest S, Mecanique non lineaire des materaux, 2001.

[24] Voisin JM, Vannes AB, Vincent L, Daviot J, Giraud B, Analysis of a tube-grid oscillatory contact: methodology for the selection of superficial treatments, Wear 181–183 (1995) 826–832.

[25] Bowden FP, Tabor D (1966) J Appl Phys 17:1521.

[26] Bucaille JL, PhD, Ecole des Mines de Paris, France, 2001, Moore DF (1972) The friction and lubrication of elastomers. Pergamon Press, London

[27] Zset software, http://www.zset-software.com

[28] Destuynder P, Djaoua M, Lescure S, Quelques remarques sur la mecanique de la rupture elastique, J. Mec. Theor. Appl. 2 (1) (1983) 113–135.

[29] Kolednik O, Schöngrundner R, Fischer F, A new view on J-integrals in elastic–plastic materials, Int. J. Fract. 187 (1) (2014) 77–107.

[30] Maurel V, Chiaruttini V, Koster A, Missoum-Benziane D, Fatigue crack growth under large scale yielding condition: a tool based on explicit crack growth, J. Theor. Comput. Appl. Mech. (2022) https://doi.org/10.46298/jtcam.9296.

[31] Prost M, Köster A, Missoum-Benziane D, Dépinoy S, Ferhat L, Rambaudon M, Maurel V, Anisotropy in cyclic behavior and fatigue crack growth of IN718 processed by laser powder bed fusion, Additive Manufacturing 61 (2023) 103301.

[32] Pook LP, Fatigue crack growth data for various materials deduced from fatigue rise of precracked plates. ASTM STP 513 (1971) 106-124.

[33] Chonghua Y, Minggao Y, A calcultation of the threshould stress intensity range for fatigue crack propagation in metals, Fatigue of Engineering Marerials and Structures 3 (1980) 189-192.

[34] Jones R, Kovarik O, Cizek J, Ang A, Lang J, Crack growth in conventionally manufactured pure nickel, titanium and aluminum and the cold spray additively manufactured equivalents, Additive Manufacturing Letters 3 (2022) 100043.

[35] Mayer H, Papakyriacou M, Zettl B, Vacic S, Endurance limit and threshold stress intensity of die cast magnesium and aluminium alloys at elevated temperatures, International Journal of Fatigue 27 (2005) 1076–1088.

[36] Lamethe JF, Sergot P, Chateauminois A, Briscoe BJ, Contact fatigue behaviour of glassy polymers with improved toughness under fretting wear conditions, Wear 255 (1–6), (2003) 758-765

[37] Ligier JL, Antoni N**,** Cumulative Microslip in Conrod Big End Bearing System, ASME 2006 Internal Combustion Engine Division Spring Technical Conference (ICES2006) (2006) 559-567.

[38] Hintikka J, Lehtovaara A, Mäntylä A, Normal displacements in non-Coulomb friction conditions during fretting , Tribology International 94 (2016) 633–639.